

High-redshift supermassive black holes: accretion through cold flows

Yu Feng,¹★ Tiziana Di Matteo,¹ Rupert Croft¹ and Nishikanta Khandai²

¹McWilliams Center for Cosmology, Department of Physics, Carnegie Mellon University, Pittsburgh, PA 15213, USA

²Department of Physics, Brookhaven National Laboratory, Upton, NY 11973, USA

Accepted 2014 March 4. Received 2014 March 3; in original form 2013 December 4

ABSTRACT

We use zoom-in techniques to re-simulate three high-redshift ($z \geq 5.5$) haloes which host $10^9 M_\odot$ black holes from the $\sim \text{Gpc}$ volume, MassiveBlack cosmological hydrodynamic simulation. We examine a number of factors potentially affecting supermassive black hole growth at high redshift in cosmological simulations. We find insignificant differences in the black hole accretion history by (i) varying the region over which feedback energy is deposited directly, (ii) changing mass resolution by factors of up to 64, (iii) changing the black hole seed mass by a factor of 100. Switching from the density–entropy formulation to the pressure–entropy formulation of smoothed particle hydrodynamics slightly increases the accretion rate. In general numerical details/model parameters appear to have small effects on the main fuelling mechanism for black holes at these high redshifts. The insensitivity to simulation technique seems to be a hallmark of the cold flow feeding picture of these high- z supermassive black holes. We show that the gas that participates in critical accretion phases in these massive objects at $z > 6$ –7 is in all cases colder, denser and forms more coherent streams than the average gas in the halo. This is also mostly the case when the black hole accretion is feedback regulated ($z < 6$), however, the distinction is less prominent. For our resimulated haloes, cold flows appear to be a viable mechanism for forming the most massive black holes in the early universe, occurring naturally in Λ cold dark matter models of structure formation, without requiring fine-tuning of numerical parameters.

Key words: accretion, accretion discs – hydrodynamics – cosmology: theory.

1 INTRODUCTION

Deep sky surveys have revealed populations of distant quasars at redshifts $z > 6$ (Fan et al. 2001, 2003, 2004, 2006; Abazajian et al. 2009; Jiang et al. 2009; Mortlock et al. 2011; Morganson et al. 2012; Willott, Omont & Bergeron 2013). The mass of the central black holes in high-redshift quasars is estimated to be $M_{\text{BH}} \sim 10^9 M_\odot$; the feasibility of growing such black holes on a time-scale of less than 1 billion years poses tight constraints on astrophysical mechanisms for doing this. Two aspects of growing such supermassive black holes are seeding and the subsequent accretion of mass. On the seeding side, seed masses from 100 to $10^5 M_\odot$ at redshifts $z > 10$ have been proposed by various authors. On the lower end, they could form from the remnants of Population III stars (Bromm, Coppi & Larson 1999; Abel, Bryan & Norman 2000; Nakamura & Umemura 2001; Yoshida et al. 2003; Gao et al. 2005; Tanaka & Haiman 2009; Tanaka, Li & Haiman 2013), or for the most massive seeds from direct gravitational collapse (Koushiappas, Bullock & Dekel 2004; Begelman, Volonteri & Rees 2006; Mayer et al. 2010; Bellovary et al. 2011; Choi, Shlosman & Begelman 2013; Latif et al. 2013).

Given a seed, the black holes must endure a sustained period of Eddington limited growth (Volonteri & Rees 2005; Lodato & Natarajan 2006; Pelupessy, Di Matteo & Ciardi 2007) to grow to masses of $10^9 M_\odot$. An important factor in studying the growth of these objects is understanding whether sufficiently strong gas inflows are present in high-redshift haloes and how self-regulation and feedback from supermassive black holes may affect them (Di Matteo, Springel & Hernquist 2005; Cattaneo & Teyssier 2007; Johansson, Naab & Burkert 2008; Booth & Schaye 2009; Mayer et al. 2010; Debuhr, Quataert & Ma 2011; Gaspari et al. 2011; Dubois et al. 2012; Hobbs et al. 2012).

Numerical simulation of the growth of supermassive black holes in a cosmological volume is a challenging problem. This is especially the case for the first quasars. Constraints from the quasar luminosity function (e.g. Fan et al. 2001) imply that such quasars are rare objects, with a density of ~ 1 – 10 Gpc^{-3} . As a consequence, to simulate the first quasars, a large volume on the order of Gpc^3 with sufficient mass resolution to resolve their host galaxies and the gas inflow within them is required.

To work around this difficulty, many authors have adopted a method of ‘resimulation’, where high resolution, ‘zoomed-in’ initial conditions are generated for high-redshift massive haloes selected from large volume, lower resolution simulations (see e.g. Li et al.

★E-mail: yfeng1@andrew.cmu.edu

2007; Sijacki, Springel & Haehnelt 2009; Hopkins & Quataert 2010; Bornaud et al. 2011; Romano-Diaz et al. 2011; Bellovary et al. 2013; Dubois et al. 2013; Anglés-Alcázar et al. 2014; Costa et al. 2014). In this commonly adopted method however the growth of the most massive black holes is then typically assumed to be associated with the most massive dark matter haloes. This may not be the case at all redshifts: it is still controversial whether halo mass is a good indicator of the black hole properties of the rare first quasars (see e.g. Kim et al. 2009; Fanidakis et al. 2013; Husband et al. 2013).

Another approach is to directly run a large volume simulation with hydrodynamics and a model for supermassive black hole formation and growth (see e.g. Di Matteo et al. 2008; Priddey, Ivison & Isaak 2008; Schaye & Dalla Vecchia 2008; Bonoli et al. 2009; Booth & Schaye 2009, 2010, 2013; Wurster & Thacker 2013). The largest simulation in this approach is the MassiveBlack (hereafter MB) simulation by Di Matteo et al. (2012), designed to study the first quasars. With a 0.75 Gpc box side length and 2×3200^3 particles, the smoothed particle hydrodynamics (SPH) simulation runs from uniform cosmological initial conditions produced around 10 supermassive black holes with $M_{\text{BH}} \sim 10^9 M_{\odot}$ at $z \sim 6$. The growth of these black holes was found to be mainly due to cold flows. Gas in the vicinity of the black holes was shown to originate from cold dense filaments that survive well within the virial radius of the halo (see also Dekel et al. 2009; Bornaud et al. 2011). Even though the mass resolution of MB is sufficient to resolve the host haloes of the first quasars, the spatial resolution was not sufficient to follow gas inflows below sub-kpc scales. Another drawback with large uniform simulations such as MB is that it becomes prohibitively expensive to experiment with the numerical schemes for hydrodynamics and feedback.

In this work we apply the resimulation method to a sample of three haloes hosting $10^9 M_{\odot}$ black holes in the hydrodynamical MB simulation. Our main goal is to study the growth of these extreme objects at higher resolution. We will examine the effect of different numerical schemes on the accretion history of black holes, then proceed to investigate how gas arrives to and participates in the growth of supermassive black holes.

The paper is organized as follows: in Section 2 we discuss the selection and construction of the initial conditions; in Section 3 we study how method of feedback energy deposition, resolution and SPH formulation affect the accretion history of the supermassive

black holes; in Section 4 we investigate in detail the picture of cold flow feeding.

2 INITIAL CONDITIONS

2.1 Selection of haloes

The MB simulation can be used to examine the relationship between black hole mass and halo mass for the entire population of hosting haloes, and this is shown in Fig. 1 at three redshifts $z = 7, 6$ and 4.75.

We can see that for the same host mass M_{halo} of a few times $10^{12} M_{\odot}$, the black hole mass can vary significantly (by greater than an order of magnitude). Similar scatter is also reported by Fanidakis et al. (2013) from semi-analytic modelling of black hole growth in dark matter simulation. The scatter shows that picking target haloes from a hydrodynamic simulation is necessary to ensure that we are sampling the distribution of supermassive black holes that we want.

We select three haloes from the MB simulation based on their black hole mass at $z = 6$. We pick three of the most massive black holes (shown as circles in Fig. 1). Their large-scale gas environment is shown in Fig. 2. The three haloes evolve differently even though they have a similar mass of a few times $10^{12} M_{\odot}$ at $z = 6$. The ranking of haloes by black hole mass can change significantly between redshifts. For example, at $z = 7$ the black hole mass in halo 2 does not even show up in Fig. 1 ($M_{\text{BH}} < 10^8 M_{\odot}$), but at $z = 6.0$ it becomes one of the most massive black holes ($M_{\text{BH}} \sim 10^9 M_{\odot}$).

We now describe the environment and black holes in each halo in turn (see also Fig. 4).

Halo 1 lies along the most prominent filament in the MB simulation (first panel in Fig. 2). The halo eventually amalgamates with nearby haloes into one ‘super halo’ that is several times more massive than any other haloes in the simulation. The most massive progenitor black hole grew rapidly at high redshift $z = 9$ via a continuous supply of cold gas flows through the filament. At low redshift the black hole mass increased due to a major merger event. Two nearby black holes are also approaching the most massive black hole, though they have not merged at $z = 4.75$ (end of simulation).

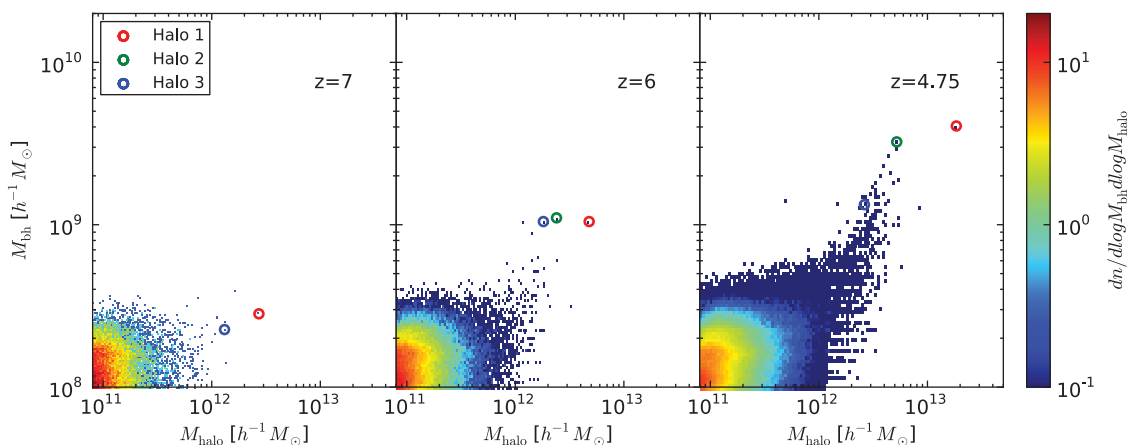


Figure 1. The mass of black holes M_{BH} compared to the total mass of their host dark matter haloes, M_{halo} . The colour in the histogram represents the number density of haloes per logarithm of black hole mass and per logarithm of halo mass. The three haloes we have targeted for resimulation are marked with coloured circles: red is halo 1, green is halo 2 and blue is halo 3. The black hole in halo 3 at $z = 7$ is not shown in the figure because its mass is less than $10^8 M_{\odot}$.

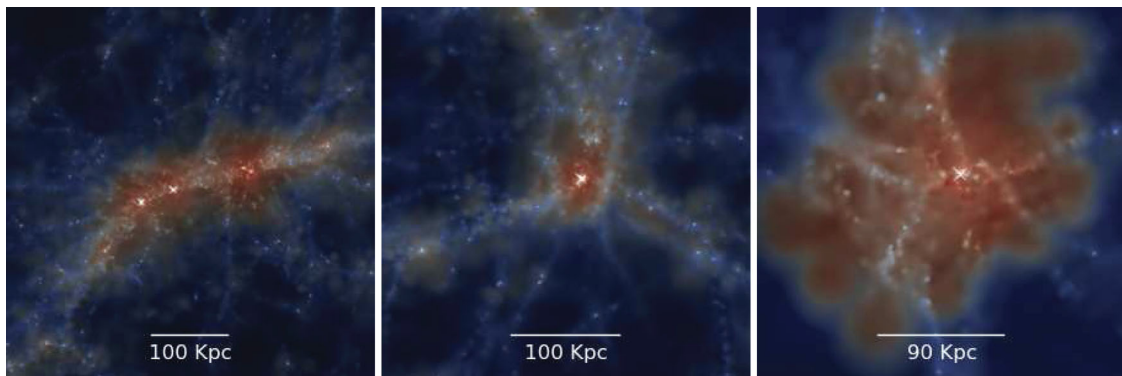


Figure 2. The environment of the haloes targeted for resimulation as seen in the MB simulation at redshift $z = 6$. From left to right: halo 1, halo 2 and halo 3. Shown is the projected gas density colour coded by temperature (red = 10^8 K, blue = 10^4 K). The scale in each panel marks the virial radius (typically 100 kpc at $z = 6.0$).

Halo 2 is located at the confluence of three filaments (second panel in Fig. 2). From a general visualization of the MB simulation (Feng et al. 2011) we can infer that this is one of the typical configurations for massive halo growth by accretion from filaments. The black hole went through a rapid growth phase between $z = 7$ and 6, when the black hole travels through a region of high-density gas ($n_b \sim 100 \text{ cm}^{-3}$).

Halo 3 is hosted by a quiescent environment. The growth of the black hole has been quenched at $z = 7$ by feedback which has reduced the cold gas supply. As we can see from the third panel in Fig. 2, the halo is surrounded by a large region of hot gas.

2.2 Generating the initial conditions

The cosmological parameters used for the initial conditions are identical to that used in MB (listed in Table 1).

Our algorithm for generating the initial conditions uses as a base the code from the initial condition generator that was used for the MB simulation (N-GENIC, author Volker Springel). This is in order to preserve the same randomly sampled large-scale Fourier modes used in MB. We modified N-GENIC to produce multiple levels of displacement at a selected region, and implemented a post-processing algorithm that assembles the particles and their displacement at different resolution levels while conserving the total mass and the centre of mass of particles.

To define the high-resolution zoom region we first find the dark matter particles in the friends-of-friends (FOF; see Davis et al. 1985) group corresponding to the selected halo at redshift $z = 6$. We then find the initial positions of these particles, and put down a bounding sphere. We enlarge the bounding sphere by a factor of 1.5, and the region inside this sphere is our highest resolution zoom region. We populate this region with high-resolution gas and dark matter particles whose initial perturbation is the sum of the interpolated (fourth-order spline) large-scale mode perturbations in the original MB initial conditions and additional small-scale mode perturbations (with random Fourier phases) drawn from smaller boxes. Outside the spherical high-resolution region, a series of spherical shells are populated with lower resolution matter particles (collisionless),

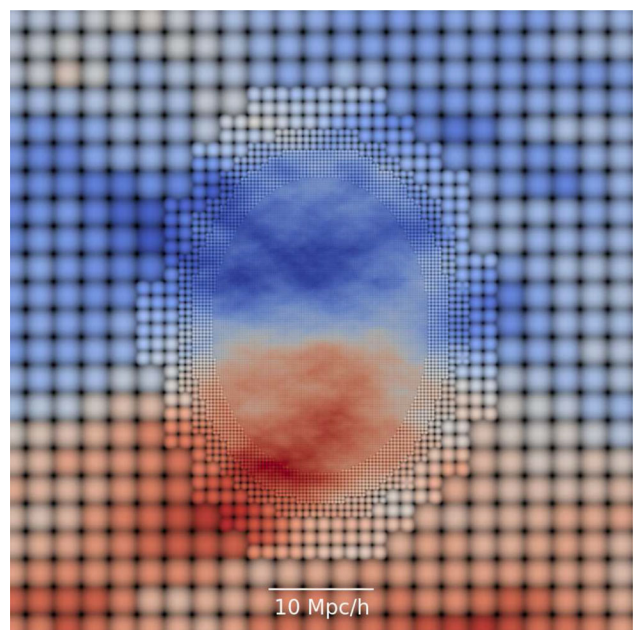


Figure 3. Illustration of gradual degrading of resolution of initial conditions with 2D projection of a slice along z -direction. Colour represents the initial Zel'Dovich x -velocity; the points represent particles: larger points correspond to lower resolution; in this particular set up, there are five resolution levels. For illustration purpose, the particles in the figure are not displaced by their initial displacement (the initial conditions). The large-scale fluctuation blends smoothly across the boundary between zoom regions as seen for the x -velocity field. The total mass and centre of mass of particles are conserved by ensuring that whenever a lower resolution particle is replaced by a higher resolution particle, it is fully replaced by eight particles (shown as four in the 2D projection).

each shell radius being a factor of 1.14 larger than that interior to it, until we have reached a spatial resolution eight times worse than that of MB. The rest of the cubical volume is populated with particles of this mass. The setup is illustrated with a 2D projection of the x -velocity field in Fig. 3.

During the simulation, we measure the minimal distance from the nearest low-resolution particle to the central black hole. The closest distance is $1 h^{-1} \text{ Mpc}$ in comoving units, which is greater than the virial radius of the halo. This provides enough evidence that particles from the low-resolution regions do not contaminate the black hole accretion and halo growth.

Table 1. Cosmology parameters.

h	Ω_b	Ω_Λ	Ω_M	σ_8	z_{init}	z_{end}
0.72	0.044	0.74	0.26	0.8	159.0	4.75

3 SIMULATIONS

Our fiducial SPH simulation code is the same as that used to run the original MB model (Di Matteo et al. 2012), P-GADGET3 (see Springel 2005, for details of the hydrodynamics and gravity computation). The formulation of SPH used in MB is density–entropy SPH (Gingold & Monaghan 1977; Lucy 1977; Springel & Hernquist 2002), with a cubic spline kernel, the black hole accretion model from Di Matteo et al. (2005) and the multiphase star formation model from Springel & Hernquist (2003). In order to assess the effects of choices for the numerical schemes, we incorporate additional features into the code:

- (i) a fixed feedback deposition volume in the black hole accretion model;
- (ii) an alternative, pressure–entropy SPH formulation to alleviate the problem of unphysical SPH surface tension (Read, Hayfield & Agertz 2010; Hopkins 2013);
- (iii) a quintic smoothing kernel to alleviate the problem of pairing instability; we also change the variable controlling the SPH resolution from N_{NGB} (number of nearest neighbours) to η (ratio between SPH resolution and mean particle separation) recommended by Price (2012) (see also Dehnen & Aly 2012).

In this work we present 18 simulations with various combinations of these models and the resolutions. The matrix of the simulations and their abbreviated names is listed in Table 2. We note that our LDCA simulations use the same model and resolution as MB; and the HDCV simulations are the simulations with the highest resolution (64 times finer mass resolution and four times finer spatial resolution than MB).

3.1 Black hole accretion model

The black hole accretion model was introduced by Springel, Di Matteo & Hernquist (2005) and Di Matteo et al. (2005). Here we summarize some relevant features. The black holes are seeded in

the simulations on-the-fly in newly formed FOF haloes with $M_{\text{halo}} \leq 5 \times 10^{10} h^{-1} M_{\odot}$. The seed mass is $M_{\text{bh, seed}} = 5 \times 10^5 h^{-1} M_{\odot}$. The accretion rate of a black hole is calculated from

$$\frac{dM}{dt} = 4\pi \min \begin{cases} A\rho(x)c_{\text{eff}}(x)^{-3}(GM)^2 & \text{Bondi scaling,} \\ Bm_p(\eta\sigma_T c)^{-1}(GM) & \text{Eddington limit,} \end{cases}$$

where the local gas density $\rho(x)$ and local effective sound speed $c_{\text{eff}}(x)$ are evaluated from the nearest neighbour SPH estimate at the black hole position x . σ_T is the Thompson cross-section, G the gravitational constant and m_p the proton mass. We have absorbed other constants in A and B . The light to mass ratio η is taken as 10 percent. We also assume that 5 percent of the light emitted becomes thermal feedback energy.

Two black holes are merged when two nearby (within the SPH resolution) black holes satisfy the condition $v_{\text{rel}} < 1/2c_{\text{sound}}$, where v_{rel} is their pairwise relative velocity and c_{sound} is the sound speed of the surrounding gas.

3.2 Merger and accretion history

When examining the accretion history of black holes in each zoom region in Sections 3.3 onward we will restrict ourselves to the most massive progenitor of the most massive black hole at $z = 6$. We find that halo 2 and halo 3 contain one central black hole each at the end of the simulation, while halo 1 contains three major black holes of similar mass. This can be seen in Fig. 4 where we show the mass evolution of the three most massive (final redshift) black holes and their progenitors in each halo. The difference in the environments of the black holes seen in Fig. 2 shows up strikingly here too, with for example halo 3 hosting only one early merger events between black holes at close to $z = 8$.

We note that where there are differences in the precise ranking of black holes for different versions of a simulation we define as the central black hole the most massive black hole in the highest resolution simulation.

Table 2. Simulation matrix. D: density–entropy formulation; P: pressure–entropy formulation; V: radius of feedback region fixed to 0.5 physical h^{-1} kpc; A: feedback region is set to 64 nearest neighbour (cubic spline) or 224 nearest neighbour (quintic spline); H, M and L stands for the resolution (high, medium and low, see text); Q: quintic spline kernel; C: cubic spline kernel.

Symbol	Halo	$\varepsilon_{\text{grav}} (h^{-1} \text{ kpc})$	$m_{\text{0DM}} (M_{\odot})$	SPH	Kernel	Feedback
1HDCV	1	1.5	4.3×10^6	DE	Cubic	Volume
1MDCV	1	3.0	3.5×10^7	DE	Cubic	Volume
1MDCA	1	3.0	3.5×10^7	DE	Cubic	Adaptive
1MDQV	1	3.0	3.5×10^7	DE	Quintic	Volume
1MPQV	1	3.0	3.5×10^7	PE	Quintic	Volume
1LDCA ^a	1	5.5	2.8×10^8	DE	Cubic	Adaptive
2HDCV	2	1.5	4.3×10^6	DE	Cubic	Volume
2MDCV	2	3.0	3.5×10^7	DE	Cubic	Volume
2MDCA	2	3.0	3.5×10^7	DE	Cubic	Adaptive
2MDQV	2	3.0	3.5×10^7	DE	Quintic	Volume
2MPQV	2	3.0	3.5×10^7	PE	Quintic	Volume
2LDCA ^a	2	5.5	2.8×10^8	DE	Cubic	Adaptive
3HDCV	3	1.5	4.3×10^6	DE	Cubic	Volume
3MDCV	3	3.0	3.5×10^7	DE	Cubic	Volume
3MDCA	3	3.0	3.5×10^7	DE	Cubic	Adaptive
3MDQV	3	3.0	3.5×10^7	DE	Quintic	Volume
3MPQV	3	3.0	3.5×10^7	PE	Quintic	Volume
3LDCA ^a	3	5.5	2.8×10^8	DE	Cubic	Adaptive

^aThe LDCA simulations use the same accretion and feedback model as MB.

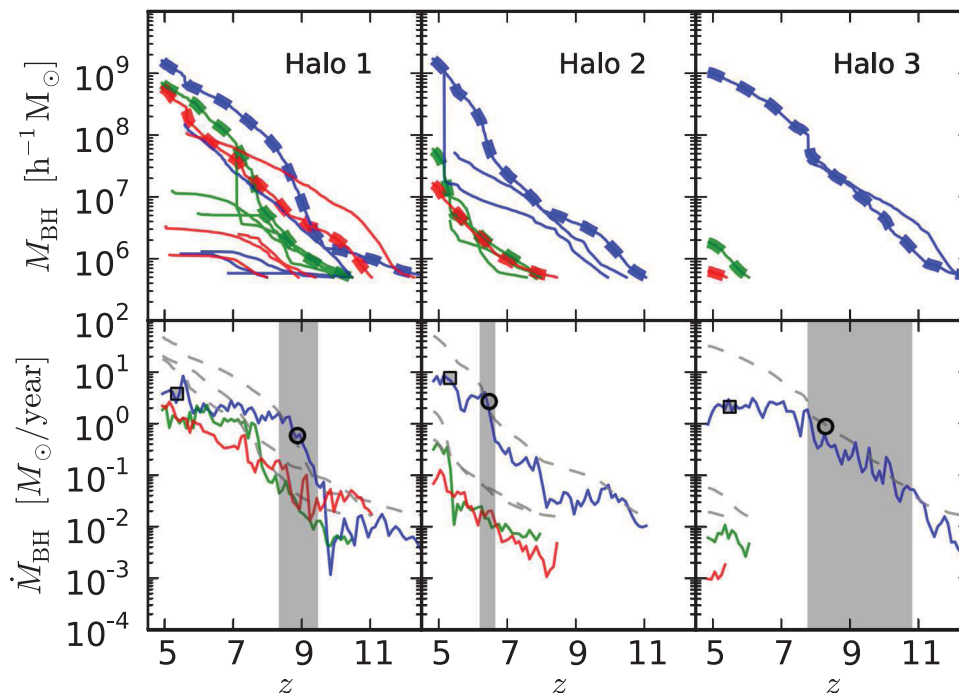


Figure 4. The merger tree of three most massive black holes in each simulated halo. The data have been taken from the simulations with the highest resolution (HDCV). From left to right we show haloes 1, 2 and 3. The thick lines show the most massive progenitors in each case; black holes in the same merger tree are shown with the same colour. The lower panel shows the accretion rate of the most massive progenitors; grey lines indicate the Eddington rate. The circles and squares mark the snapshot redshifts at which the particles used in the EA phase and RA phase analysis are selected in Section 4. The shaded area shows the duration of the EA phase.

In the following subsections we explore the effect of varying the accretion and feedback models on the growth of the central black hole.

3.3 Deposition of AGN feedback energy

The black holes deposit feedback energy into nearby gas environment. In our simulations, we model this process by depositing thermal feedback energy to the neighbouring gas particles, weighted by their mass. The exact details of the physical mechanism by which this occurs in real galaxies are likely dictated by radiative transfer through the medium surrounding the black hole (Hayes et al. 2006; Ciotti & Ostriker 2007; Alvarez, Wise & Abel 2009; Milosavljević, Couch & Bromm 2009; Park & Ricotti 2011, 2012; Jeon et al. 2012; Novak, Ostriker & Ciotti 2012). As the length and mass scales over which this occurs are not certain, it is important to test how our sub-grid prescription for depositing this feedback energy affects growth of the black holes.

In the original MB simulation the energy deposition was done using the SPH smoothing kernel of the black hole particle to distribute energy to the 64 nearest neighbours. We refer to the MB feedback method ‘adaptive’, as the size of the feedback region is directly proportional to the mean separation of SPH particles close to the black hole (a ratio of $\eta = 1.26$). In order to preserve the ratio, we use 224 neighbours in the quintic spline kernel simulations.

An alternative to the ‘adaptive’ model is to fix the proper volume of the gas receiving the feedback energy. For the fixed-volume model, we use a region corresponding to a spline smoothing kernel with proper radius $h = 0.5 h^{-1}$ kpc. The total mass of gas receiving the feedback energy is therefore proportional to the gas density around the black hole. Note that we do not use the fixed-volume

model at low resolution as the feedback region is smaller than the gravitational smoothing when even at very high redshift ($z < 10$).

In Fig. 5, we compare the results of simulations with the adaptive model for distributing feedback energy and those with the fixed-volume model at the medium resolution (MDCA and MDCV simulations in Table 2). We can see that the black hole mass, accretion and the halo star formation in all three haloes are very similar for both feedback models (within the same order of magnitude). The only exception is in halo 1, where there is some difference in the early growth: the accretion rate in the adaptive model remains two orders of magnitude lower than the fixed-volume model until redshift $z = 8.5$. The difference in accretion rate disappears after $z < 8$, and eventually the black hole mass between two models become very similar. The star formation in the halo also experiences a burst during the same period, indicating an accumulation of cold dense gas in the halo before the black hole accretion kicks in. After the accretion is started, the black hole mass quickly picks up. We therefore regard the similarity in the late time black hole masses and accretion rates as more definitive. The choice of feedback region therefore does not appear to significantly alter the accretion history.

3.4 Resolution

The MB simulation has a gravitational force softening length of $\varepsilon = 5.5 h^{-1}$ kpc. The resimulations are conducted with three different gravitational force softening lengths (in comoving coordinates): 5.5 (low resolution), 3.0 (medium resolution) and $1.5 h^{-1}$ kpc (high resolution). Our highest resolution simulation therefore has a proper resolution of 300 pc at $z = 6$. The simulations do not resolve the influence sphere of the supermassive black holes, which has a radius close to 50 pc at $z \sim 6$. This is consistent with the model used in

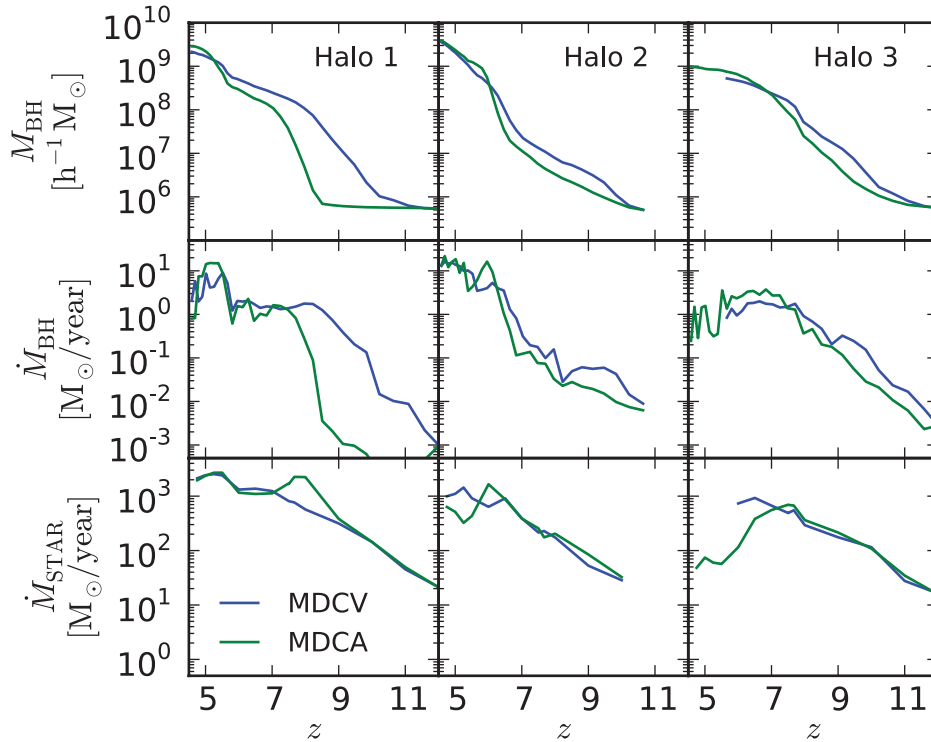


Figure 5. The dependence of black hole accretion history on feedback energy deposition prescription. From left to right we plot haloes 1, 2 and 3. The blue curves show results for the fixed-volume (finite physical radius of $0.5 h^{-1}$ kpc) feedback kernel. The green curves are for the fixed-mass kernel, which uses the 64 nearest neighbours. We also show the star formation rate of the halo in the bottom panels. Refer to the text in Section 3.3.

this work, which was calibrated for a subgrid treatment of the black hole vicinity (see e.g. Di Matteo et al. 2008).

We plot the accretion history for the three different black holes at different resolutions in Fig. 6, showing black hole mass and accretion rate and the star formation rate in the halo. We find that the resolution does not appear to be affecting the black hole growth and the star formation in the halo. The accretion history appear to have reached convergence with the medium-resolution simulations (MDCV and MDCA), which shows no significant difference with the high-resolution simulations (HDCV) that has eight times better mass resolution. We also note that in the resimulations, the suppression in star formation rate is tightly coupled with the suppression of black hole accretion, in agreement with Khandai et al. (2012). The level of suppression varies from case to case. We attribute the variance to the difference of amount of black hole feedback: the simulations with more massive black holes are in general associated with strong suppression in star formation. At high redshift when both black hole and star formation are determined by the cold gas supply, the star formation shows very good agreement.

The major difference again lies in the adaptive feedback model. We see that the initial growth ($z > 8$) of the adaptive model shows stronger resolution dependence than the fixed-volume model in both halo 1 and halo 3: the lower resolution simulation (LDCA) produces slower initial growth at $z > 8$ than the higher resolution (MDCA). The difference in halo 3 is less drastic than the difference in halo 1 and is not associated with a burst in star formation rate. We believe this is because the halo is in a relatively isolated region, and the cold gas supply is lower than halo 1.

We point out that eventually ($z < 6$) the lower resolution simulation (LDCA) does also reach the same final black hole mass as the

medium-resolution simulation (MDCA), with the dependence on resolution disappearing. This is because at $z < 6$ the black hole is sufficiently massive that the accretion becomes regulated by feedback, regardless of how the feedback is implemented.

3.5 SPH formulation: pressure–entropy

Recent developments in SPH include the introduction of the so-called pressure–entropy formulation (Read et al. 2010; Hopkins 2013), and the quintic smoothing kernel (Price 2008). These new developments aimed to address several difficulties noticed in prior formulations of SPH, namely: an unphysical surface tension across surface boundaries that forbids particle exchange at a density discontinuity, the fluctuation in density estimation due to a small number of nearest neighbours (32) and nearby particles bonding into pairs causing a loss of resolution in high-density regions (see e.g. Schuessler & Schmitt 1981; Morris 1996; Monaghan 2000; Agertz et al. 2007; Wadsley, Veeravalli & Couchman 2008).

We have run our zoomed simulations with pressure–entropy SPH and the traditional density–entropy SPH formulation. The black hole accretion histories and the halo star formation rates are shown in Fig. 7. We can see that going from density–entropy to pressure–entropy formulations appears to consistently result in faster black hole accretion. The star formation history is largely intact, although with some variance in the level of suppression at low redshift (see discussion in the previous section). Comparing the results for quintic spline and cubic kernels (both are plotted) we can see that some of the contribution to the faster black hole accretion is due to the switch to a quintic spline kernel. The quintic spline kernel samples more particles (112) and reduces the noise in the quantities used

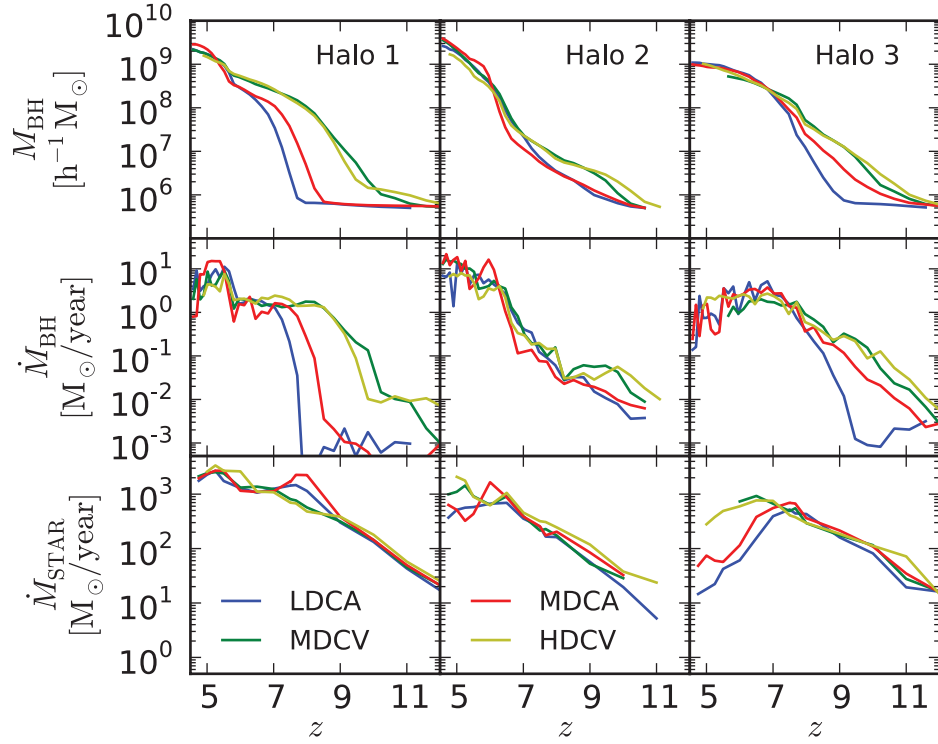


Figure 6. Resolution dependence of the accretion history of the most massive black holes in our three selected target haloes. From left to right we plot halo 1, halo 2 and halo 3. The blue (LDCA) curves are the lowest resolution, green and red (MDCV, MDCA) are medium resolution and yellow (HDCV) is high resolution (see Section 3.4).

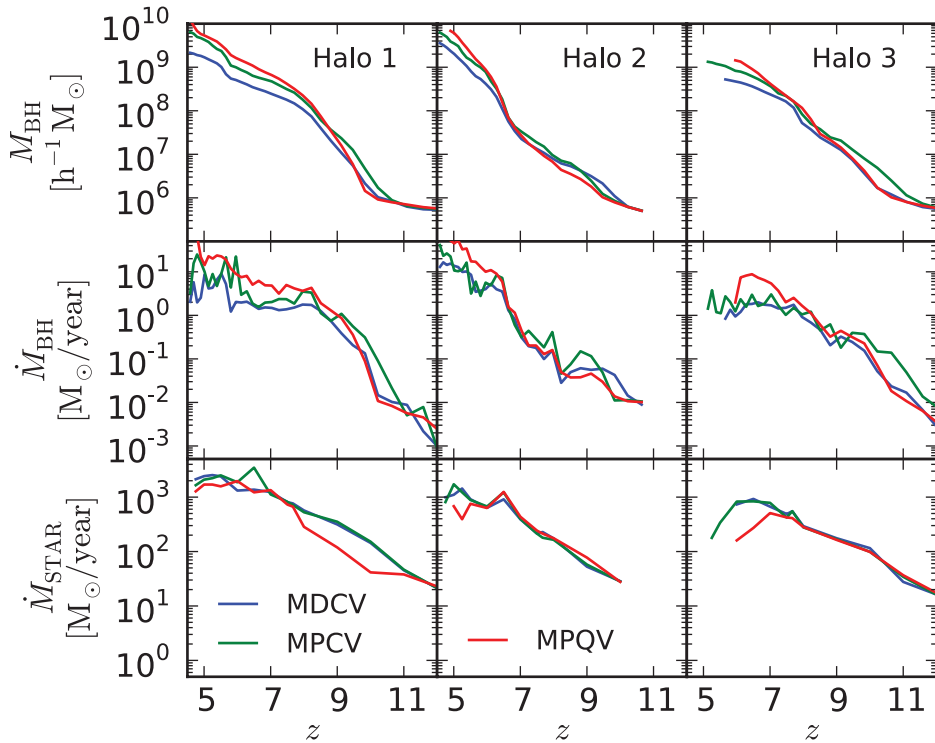


Figure 7. The effect of changing SPH formulation on the accretion history of the black holes. From left to right we show halo 1, halo 2 and halo 3. The blue (MDCV) line is the density–entropy formulation with a cubic spline smoothing kernel, the green (MPCV) line is the pressure–entropy formulation with a cubic spline smoothing kernel and the red (MPQV) line is the pressure–entropy formulation with quintic spline smoothing kernel.

the black hole accretion model. The black holes are up to a factor of 5 times more massive at the final time in the pressure–entropy case compared to density–entropy case. We note that there is a free parameter in the black hole model, namely the feedback efficiency (set to 10 per cent here). This parameter was set (Di Matteo et al. 2005) to reproduce black hole masses observed in the local Universe and so with pressure–entropy SPH a recalibration of this parameter could be employed.

3.6 Seeding mass

The origin and nature of the black hole seed population remain uncertain. Two distinct populations of black hole seeds, in the range of $100\text{--}10^6 M_\odot$, have been proposed, either from the remnants of the first generation of Population III stars at $z \sim 20\text{--}30$ or from direct dynamical collapse of gas. In large volume cosmological simulations such as MB it is not currently possible to resolve the collapse of the (small mass) haloes at redshifts commensurate with black hole seed formation and hence resolve these processes directly. As a result, the black hole seed mass is a parameter of our models (see also Costa et al. 2014), and the early growth phase cannot be accurately followed.

In this section we explore the effect of changing our black hole seed mass on the growth of the first quasars. We have performed a series of resimulations of halo 2, where we decrease the seed mass by up to a factor of 100. In particular, we use $M_{\text{seed}} = 5 \times 10^3$ (M3), 5×10^4 (M4), $5 \times 10^5 h^{-1} M_\odot$ (M5) and seed them in haloes of $M_{\text{halo, seed}} = 5 \times 10^8, 5 \times 10^9, 5 \times 10^{10} h^{-1} M_\odot$, respectively. In these zoom runs, we are limited by the minimum mass of a resolved halo (which corresponds to $10^8 M_\odot$ in the medium-resolution simulations): reducing the black hole seed mass further (e.g. closer to $100 M_\odot$) would require resolving haloes of the order of $10^6 M_\odot$ commensurate with those forming first Population III stars. We show the accretion history and star formation history in Fig. 8.

The accretion history in the simulations with different seed mass follows a similar growth history. In general, by lowering the seeding mass,

- (i) the early ($z > 8$) growth of the supermassive black hole is somewhat suppressed;
- (ii) the early star formation history is neither enhanced or suppressed, indicating that black hole accretion and associated feedback are not affecting the gas supply for star formation;
- (iii) smaller black holes are seeded earlier due to the reduced seeding halo mass; the earlier seeding compensates for the smaller seeding mass, and the black hole undergoes a longer Eddington growth period;
- (iv) eventually, regardless of the mass of the seed, the black holes grow to a final mass of about $10^9 M_\odot$.

In conclusion, we observe no significant change to the black hole accretion history in our simulations as long as a reasonable seeding mass is used.

4 FEEDING BLACK HOLES VIA COLD FLOWS

We now investigate the fuel supply on to black holes and study the thermal history of high-redshift gas that participates in black hole accretion. We focus on the question of whether the gas that fuels the black hole is different from the typical gas in the halo. We want to further test the indication that at these high redshifts ($z \sim 6$) fast black hole growth can be achieved via cold flows (Di Matteo et al.

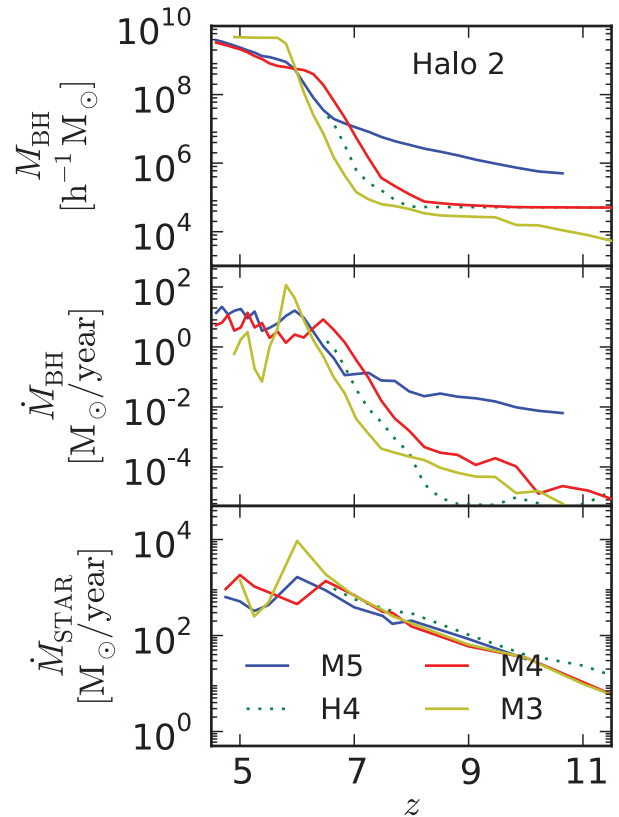


Figure 8. The dependence of black hole accretion history on seeding mass. The blue (M5), red (M4) and yellow (M3) represent the simulation at medium resolution with seeding mass of 5×10^3 , 5×10^4 and $5 \times 10^5 h^{-1} M_\odot$. H4 (green dotted line) represents a high-resolution simulation that is run to redshift 6.5.

2012). Further we aim to investigate how black hole feedback may play a role in disrupting the cold streams close to the black hole.

The virial temperature of the hosting halo of $10^{12} M_\odot$ is close to 10^6 K, while in the simulation the cold intergalactic medium (IGM) temperature is close to 10^4 K. We set the split between hot and cold gas at 10^5 K. In Fig. 9, we compare the morphology of the cold gas ($T < 10^5$ K) and that of the hot gas ($T > 10^5$ K) around the black holes in the three haloes. We first notice that the cold gas forms dense compact filaments that are unlikely due to resolution effects: as we increase resolution, the cold gas filaments are identical in morphology except have increased sharpness. Secondly, we notice that the hot gas is distributed in a diffuse manner, forming thicker structures containing large blobs that extend to the entire halo.

The striking morphological difference between hot and cold gas motivates us to consider two species of gas particles.

- (i) The first gas species we call ‘HALO’ particles¹ and are randomly selected gas particles from the halo, weighted by volume; because hot gas particles occupy most of the volume of the halo, HALO particles are most likely the hot environment gas in the halo shown in the bottom panel of Fig. 9.

¹ Not to be confused with the dark matter particles in the halo.

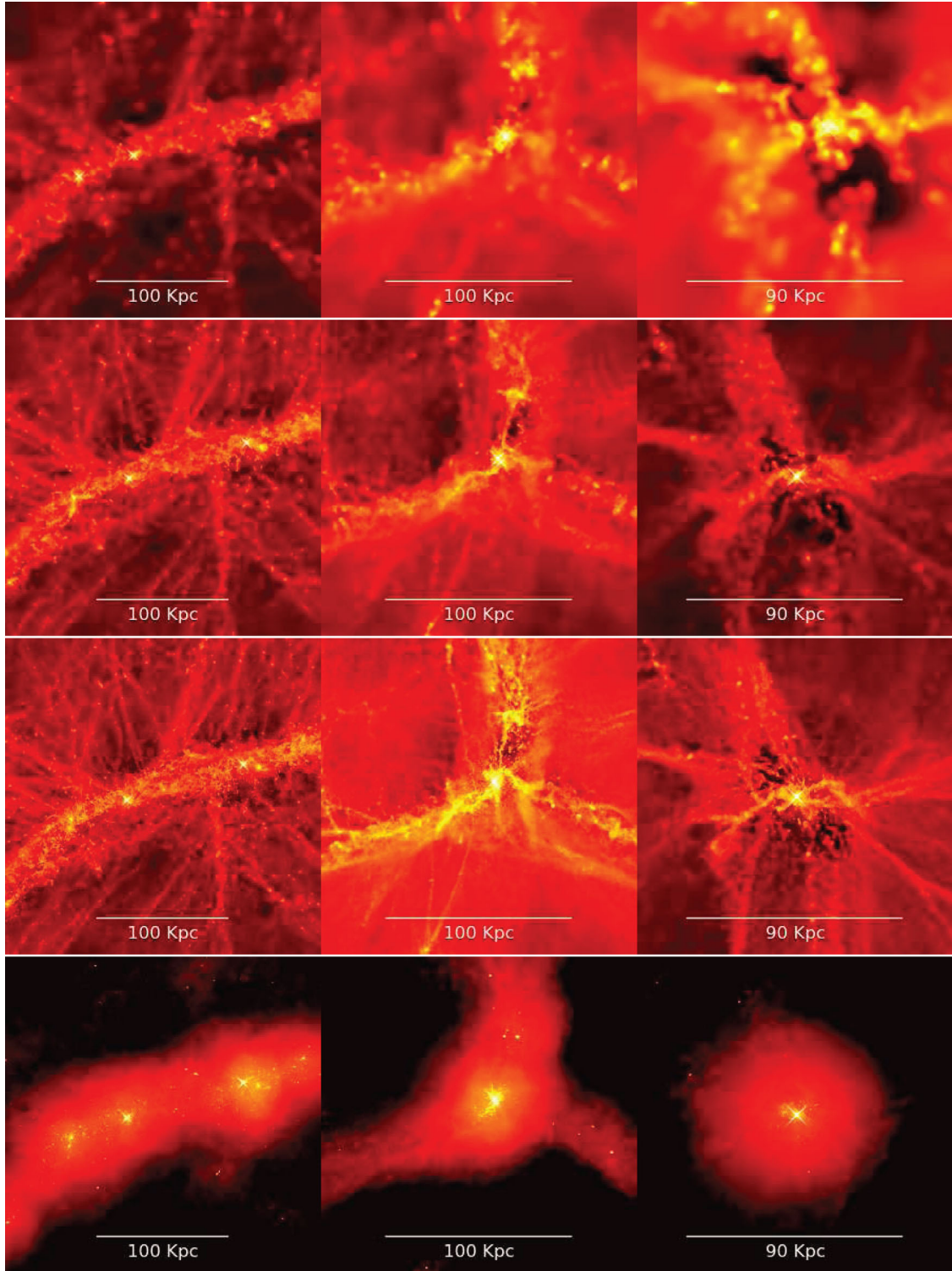


Figure 9. Top three rows: cold gas filaments surrounding black holes in the simulations, run at different resolution. The colour represents the projected density (in a cube) of cold ($T < 10^5$ K) gas at $z = 6.5$. The columns show haloes 1, 2 and 3, from left to right. The first three rows are, from top to bottom, low resolution, medium resolution and high resolution. The bottom row shows the density distribution of the hot gas in the high-resolution simulation.

(ii) The second gas species are the ‘BH’ particles,² and are the nearest neighbour particles contributing to the evaluation of gas

properties at the black hole. The BH particles are the gas particles that are actively participating in accretion on to the black hole.

² Not to be confused with particles that represent the black holes in the simulation.

After a gas particle (if it has not been converted to a star particle) enters the halo, depending on its cooling efficiency, the particle will either be heated to the virial temperature of the halo, losing

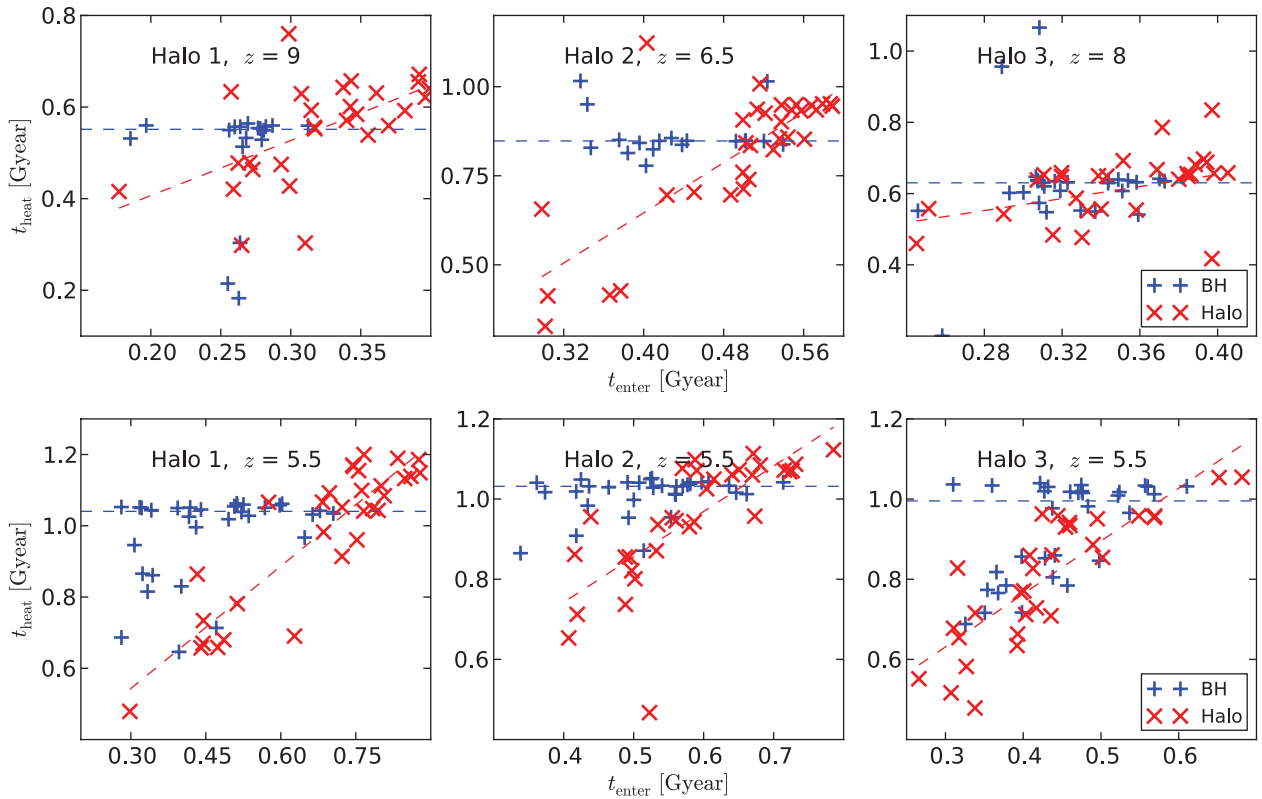


Figure 10. Time since the big bang that a particle enters a halo (t_{enter}) plotted against time since the big bang for a particle to heat up to the virial temperature (t_{heat}). HALO particles and BH particles (see text) are shown in red and blue, respectively. The panels show haloes 1, 2 and 3 from left to right. The upper panels are at the EA phase when the black holes are undergoing Eddington accretion. The lower panels are in the RA phase when the black hole growth is regulated by feedback. The red horizontal dashed line indicates the time when most of the BH particles are heated, acting as a visual guide to the time-scale of black hole heating. The blue dashed line is a linear fit to the HALO particles, visually guide the time-scale of halo heating.

its initial inflow motion, or remain cold, arriving to the centre of the halo to participate in star formation and black hole accretion. In this picture, the history of a gas particle can be quantified by two characteristic times:

- (i) the entering time t_{enter} , the time since the big bang at which a gas particle first enters the virial radius;
- (ii) the heating time t_{heated} , the time since the big bang at which a gas particle is first heated above the virial temperature of the gas.

We also calculate the correlation coefficient (CC) of the two characteristic times:

$$CC = \rho_{X,Y} = \frac{\text{cov}(X,Y)}{\sigma_X \sigma_Y} = \frac{E[(X - \mu_X)(Y - \mu_Y)]}{\sigma_X \sigma_Y},$$

where X and Y represent t_{enter} and t_{heated} , σ and μ the standard deviation and the mean of the data and E the mean operator.

CC measures the correlation between the time a gas particle enters the halo and the time a particle is heated to the virial temperature of the halo. If a particle is heated by the virial heating from the halo, we expect CC to be large, for particles entering the halo early shall be heated early, while those entering late shall be heated late. On the other hand, if a particle is heated by the central black hole, we expected CC to be small, for these particles are heated only after they arrive to the black hole, no matter when they enter the halo. As we will show later, these expectations agree with our simulations.

We calculate t_{enter} , t_{heated} and CC for BH and HALO particles at two epochs from the high-resolution simulations (HDCV): (1) the first epoch is when the black hole is undergoing Eddington accretion (EA phase, $\dot{M}_{\text{BH}} \sim \dot{M}_{\text{Edd}}$), and (2) the second epoch is when the

black hole accretion has been regulated (RA phase, $\dot{M}_{\text{BH}} \ll \dot{M}_{\text{Edd}}$). The EA phases of three haloes are marked with shaded areas in Fig. 4. We choose the particles in redshifts selected a priori (without the knowledge of the behaviour of particles) at $z = 9$, 6.5 and 7.5 for each halo respectively to perform the analysis. Similarly, in the RA phase analysis, we use the particles at redshift of $z = 5.5$ for all three haloes.

The results are shown in Fig. 10 and Table 3. We first look in the EA phase. During the EA phase, the CC between the heating time and entering time of the BH particles is much smaller than that of the HALO particles as seen in the first row in Table 3. The difference can also be seen in Fig. 10, where the BH particles are clustering around the same t_{heated} that corresponds to the time the particle becomes the nearest neighbour of the black hole, while the HALO particles follow a line with a positive slope. The lower CC in BH particles is consistent with heating by black hole feedback: the BH particles remain cold after they enter the halo, and are then heated up shortly after they arrive at the black hole. The larger CC with HALO particles in EA phase is consistent with the virial

Table 3. Correlation coefficient (CC) between t_{heated} and t_{enter} . Also see Fig. 10.

	Halo 1		Halo 2		Halo 3	
	BH	HALO	BH	HALO	BH	HALO
EA (high redshift)	0.069	0.574	-0.075	0.778	0.131	0.337
RA ($z = 5.5$)	0.389	0.893	0.356	0.745	0.557	0.827

heating picture: the hot gas halo is formed by virial heating from the halo (which may indirectly contain the feedback energy from the central black hole and the feedback energy from satellites); if a HALO particle enters the halo early, it is also heated early.

This difference suggests that the gas that participates the black hole accretion in an Eddington accretion phase is unlikely to be from the hot halo environment. The gas must have come directly from outside of the halo; and its thermal history is consistent with that of the cold flows.

We then move on to the RA phase, during which black hole accretion has been regulated. We notice that the CC of the BH particles have significantly increased. In the lower panels of Fig. 10, we find this increase is due to a larger population of the BH particles that behave similarly to the HALO particles. The existence of a HALO-like population within the BH particles shows that the cold flows (though they still exist) are being somewhat disrupted. Because the HALO-like particles are heated before they arrive to the black hole, the temperature around the black hole rises, and the black hole accretion is regulated.

We investigate further the motion of BH particles and HALO particles in the RA phase with Figs 11–13. In Fig. 11, we plot the history of properties of BH and HALO particles in simulation 1MDCV, where we saved one snapshot every 3 Myr of simulation time. In this case we have traced 32 particles of each population originating from three snapshots close to $z = 5.5$ (three columns are three snapshots; two rows are BH and HALO from top to bottom, note that the time increases from right to left). The considered properties are the following.

- (i) T : the temperature of the particle; we compare the temperature with the virial temperature of the halo.
- (ii) r : the distance between the particle and the black hole (proper); we compare the distance with the virial radius of the halo.
- (iii) v_r : the radial velocity of the particle; negative value ($v_r < 0$) is infalling and positive ($v_r > 0$) is outflowing.
- (iv) n : the density of the particle.

We visualize the history of each property with a 2D histogram binned by the quantity and time in Fig. 11. The histogram demonstrates the behaviour of the entire population as a function of time: the particles with similar property at a given time will contribute to the same bin, resulting a darker pixel. For example, the dark horizontal line at $T = 10^4$ K in the top panel T plots of Fig. 11 indicates a large fraction of gas remains cold for a very long time. We also mark the probability distribution of t_{heated} and t_{enter} in the figure. We are more interested in the behaviour of the gas between t_{enter} and t_{heated} .

In the three top panels for BH particles, we see that most of the BH particles have significantly increased their density while remaining cold for as long as 0.5 Gyr after they enter the halo, as suggested by the dark lines in T , v_r and n . We do notice that for some of the particles, the infalling motion starts to become disrupted much sooner (0.2 Gyr after entering), while their temperature rise to the virial temperature. As we will see after analysing the HALO particles, this early heating population within BH gas is very similar to the HALO particles: they correspond to the HALO-like population we identified in the lower panels of Fig. 10, which are responsible for the increased correlation between t_{enter} and t_{heated} . The population indicates that the cold flows in a regulated growth phase are being disrupted, and can no longer provide the Eddington accretion of black holes. All of the BH particles are heated after they get close to the black hole ($r < 1$ kpc), but the temperature reaches up to 10^8 K,

much higher than the virial temperature of the halo (10^7 K) at this redshift. Some of the heated particles can receive an outflowing velocity up to 1000 km s^{-1} , and can reach a substantial distance away from the black hole, though none of the heated particles have reached a distance further than the virial radius of the halo. We do note that our method cannot exclude the possibility that a fraction of heated particles escape from the halo. We plan to investigate whether any of the BH particles is unbound from the halo due to feedback from the black hole in a further study.

In the three low panels for HALO particles, we see that the heating happens much sooner (within 0.2 Gyr) after they enter the halo. The infalling motion is disrupted as the particles are heated, and most of the particles remains at a low density of 10^{-6} cm^{-3} . After being heated, the temperature of HALO particles tightly tracks the virial temperature of the halo, as the halo grows.

We proceed to visualize the motion of the inflowing gas with Fig. 12 for the particles selected from the three snapshots near $z = 5.5$. In Fig. 12, we show the trajectories of the BH and HALO particles projected in the x - y plane, coloured by their temperature. The BH particles, being initially cold ($T \sim 10^4$ K), flow into the black hole (located at the centre of the plots), apparently following several preferred directions. The majority of the BH particles remain cold until they arrive to the black hole. However, we can also see some of the particles are heated to $T > 10^6$ K before arriving the black hole; these particles correspond to the HALO-like particles. Afterwards, the particles are ejected towards directions that are unaligned to the directions they come in from. The ejected gas can reach 100 kpc away from the black hole, though still within the virial radius of the halo. The HALO particles show a very different pattern. Although the HALO particles are also initially cold ($T \sim 10^4$ K), the gas is quickly heated to the virial temperature of the halo ($T \sim 10^6$ K). Afterwards, the motion of particles visually resembles a random walk within the virial radius of the halo (a few times 100 kpc).

The fate of BH particles in the EA phase is drastically different. As shown in the top panels of Fig. 13, we see that instead of being ejected away, most of the BH particles remain cold after arriving at the black hole and they are eventually consumed by black hole accretion and star formation at the very centre of the halo. The fate of HALO particles in the EA phase is rather similar to that in the RA phase: particles are heated to the virial temperature as they fall into the halo.

5 CONCLUSION

We have studied the fuelling and gas supply on to high-redshift supermassive black holes in high-resolution resimulations of haloes selected from the MB hydrodynamic cosmological simulation (covering a volume close to 1 Gpc^3). Using MB, Di Matteo et al. (2012) showed that steady high-density cold gas flows were able to produce the high gas densities that can lead to sustained critical (Eddington) accretion rates and hence rapid growth commensurate with the existence of $10^9 M_\odot$ black holes as early as $z \sim 7$. We have tested this scenario further for a subsample of three of the haloes hosting $10^9 M_\odot$ black holes at $z = 6.0$ in MB. We have used zoom-in techniques to investigate the nature of the gas inflows at scales that could not be resolved from the large volume MB simulation.

We have shown that for the three resimulated haloes the growth history of their central supermassive black holes is consistent with a sustained Eddington limited fuelling provided by cold streams of gas that penetrate all the way to the innermost region of the galaxies undisrupted (i.e. consistent with our earlier picture). Our

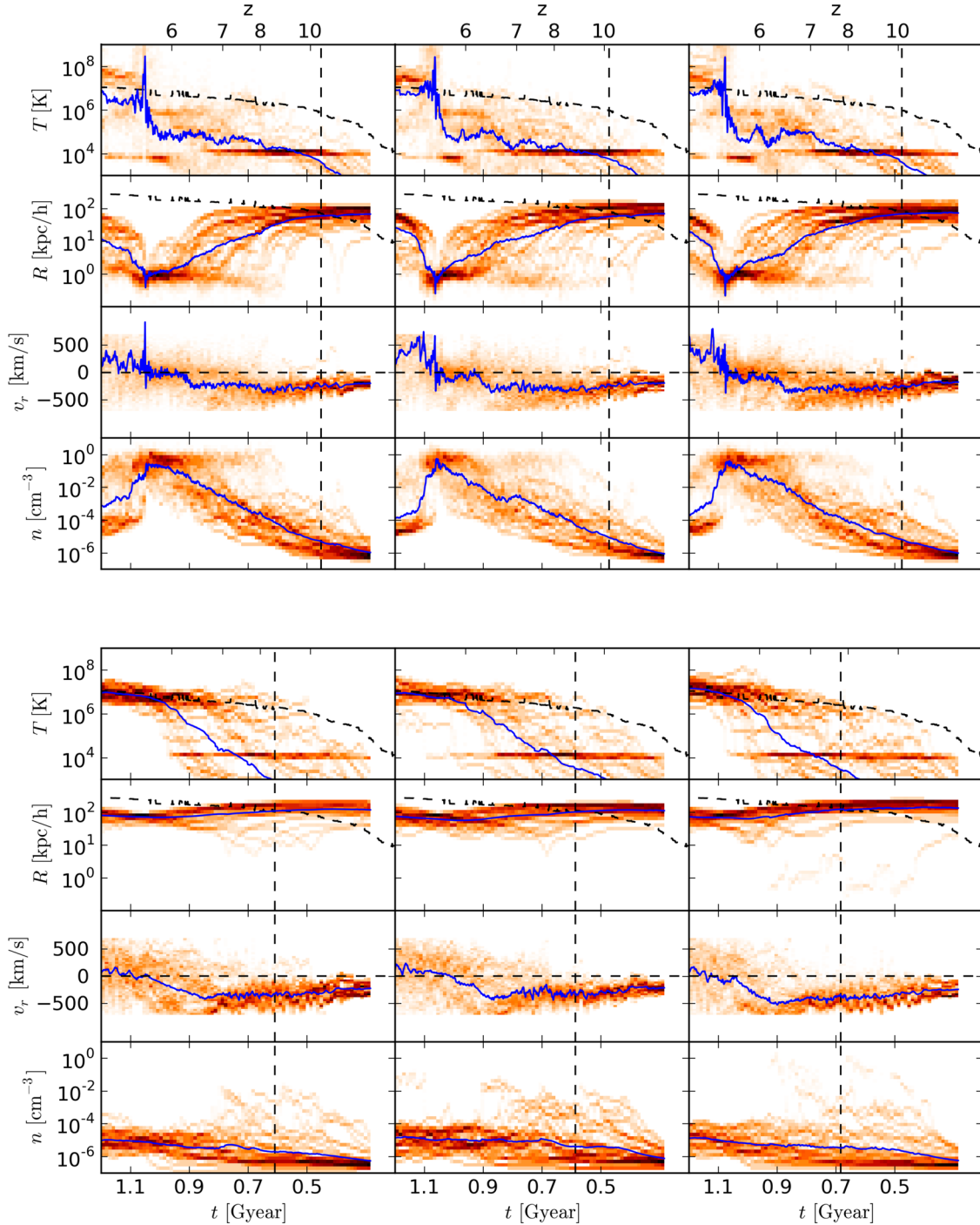


Figure 11. The properties of HALO and BH particles selected from three snapshots close to $z = 5.5$, as function of time. Top row: BH particles (nearest neighbours of the black hole). Bottom row: HALO particles (randomly picked from inside the halo). The subpanels with in a figure are the following: temperature (T), distance to black hole (r), radial velocity (v_r) and density (n). The 2D histogram visualizes the trajectories of particles, with the mean value shown in blue solid lines (see text). The black dashed lines mark the virial temperature, virial radius and zero radial velocity. The black vertical lines mark the average of the time a particle enters the halo (t_{enter} , see text).

conclusions remain unchanged even though the numerical scheme we use is varied in several significant aspects:

- (i) a change in resolution does not change the fuelling history;
- (ii) active galactic nuclei (AGN) feedback energy is spread over different size regions of constant mass or volume;

- (iii) an improved formulation of SPH (pressure–entropy and quintic kernel) is used (in this case, the growth of the black holes is systematically faster);

- (iv) the black hole growth history is insensitive to changes of the seed black hole mass (in the range of $M_{\text{seed}} = 5 \times 10^3 - 5 \times 10^5$, commensurate with the simulation resolution).

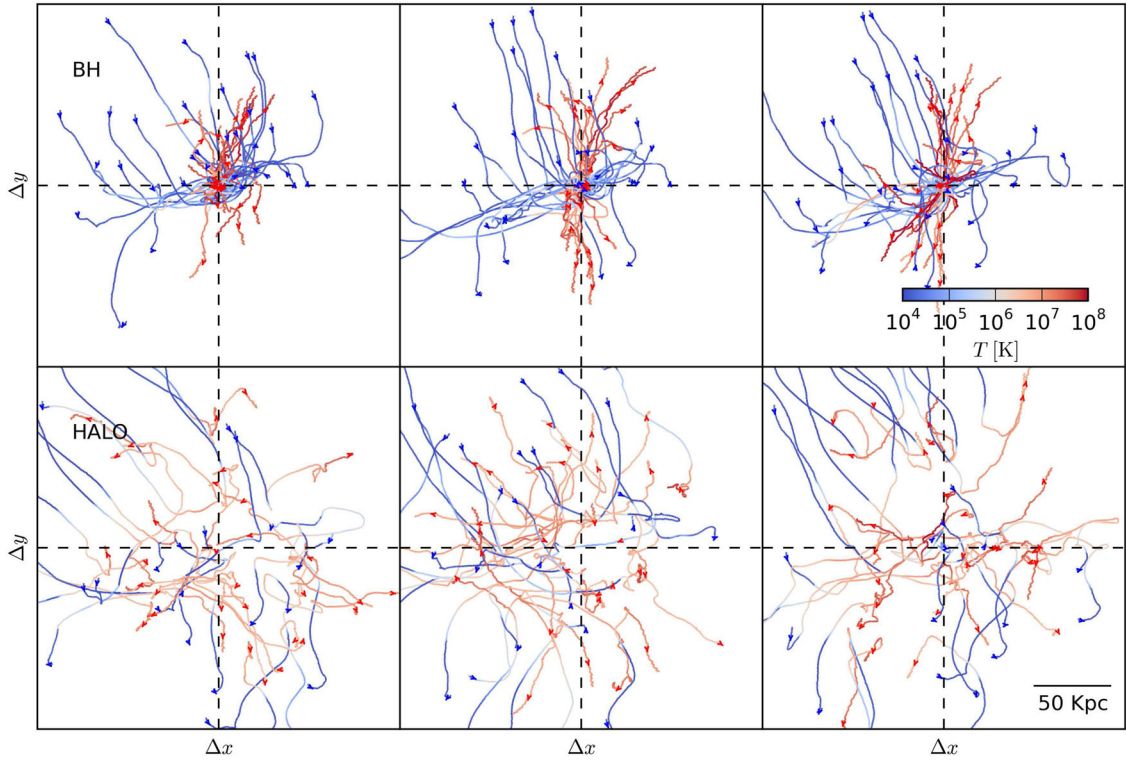


Figure 12. The trajectories of BH and HALO gas particles, projected into the x - y plane, during the RA phase. Top panels: BH particles that participate in accretion on to the black hole. Bottom panels: HALO particles. The trajectories are colour coded by temperature: red is 10^8 K; blue is 10^3 K. The wedges show the direction of motion.

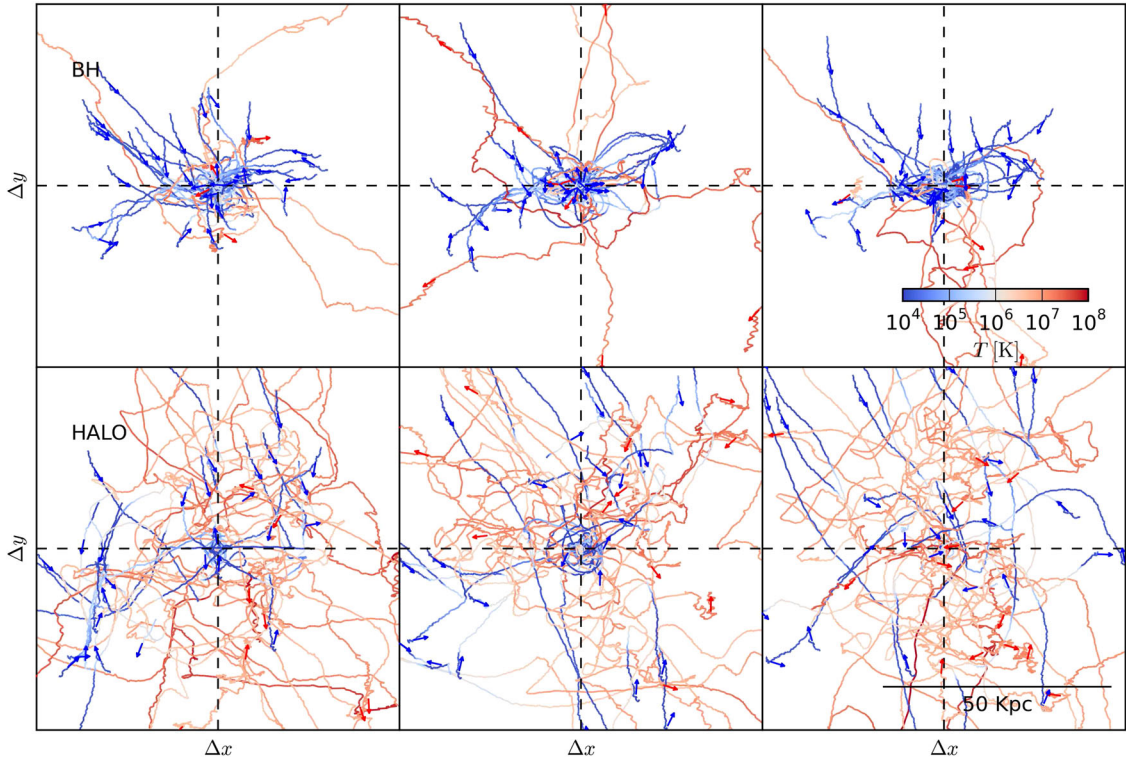


Figure 13. The trajectories of BH and HALO gas particles, projected into the x - y plane, during the EA phase. Top panel: BH particles that participate in accretion on to the black hole. Bottom panel: HALO particles. The trajectories are colour coded by temperature: red is 10^8 K; blue is 10^3 K. The wedges show the direction of motion.

There were several recent studies on the supermassive black holes based on the resimulation method. For example, Costa et al. (2014) applied a similar resimulation method to 18 haloes selected from the Millennium Simulation (dark matter only) and reported that haloes in large scale over dense regions are able to experience critical growth commensurate with $10^9 M_\odot$ by $z = 6$. Our results are in consistency with Costa et al. Bellovary et al. (2013) also studied the growth history of black holes in high-redshift haloes. Their zoomed regions were extracted from an initial cosmological box of only 50 Mpc per side, unlikely to contain high enough over dense regions. We note that their final black hole masses are consistent with what is expected from more moderately overdense regions, such as those studied by Costa et al. (2014).

We have investigated the nature of the gas fuelling the central black holes by computing the correlation between the time required for gas particles (in the halo) to reach the virial temperature and the time since they first enter the halo. We also investigated the correlation of gas participating in accretion and the correlation of the hot gas in the halo environment. We have found that while gas that fuels the black hole preserves its low temperature until heated by the feedback from the black hole (low correlation), the gas ending up in the halo environment typically heats quickly upon entering the halo (high correlation). With this method, we have shown that during the Eddington growth phase, the accretion gas appears to have directly arrived to the black hole through cold flows without disruption from the hot environment; while during the regulated growth phases ($z < 6$) a larger population of the accretion gas behave very similar to the hot environment, indicating that the cold flows are becoming disrupted by the feedback.

After being heated by the black hole the gas particles are ejected with a high velocity up to 1000 km s^{-1} from the black hole, though none of the particles we have investigated has left the halo. Several authors (see e.g. McCarthy et al. 2011; Dubois et al. 2013) reported that the strong outflows during the regulated phase at high redshift can reduce the baryon fraction in the halo up to 30 per cent, increasing the entropy of haloes at lower redshift. In our haloes, the disruption appears to be not as strong, as most of the gas surrounding the black hole is cold even after the accretion is regulated. One possible source of the discrepancy is that their haloes are less massive, and the supply of cold gas is less efficient: for example, our smallest halo (halo 3) has the largest fraction of HALO-like gas population which is heated before they arrive to the black hole. We note that the faster black hole accretion in pressure–entropy formulation suggests a higher feedback efficiency, which may contribute to the disruption of cold flow and produce a stronger hot outflow. We plan to investigate the hot outflows with further studies.

We have not evaluated the effects of resolving into the black hole zone of influence for our black holes. It is unclear whether the accretion model we used requires a recalibration. Modelling the zone of influence may require more detailed treatment of the physics processes, such as radiative transfer. Our simulations were only able to resolve haloes more massive than $\sim 10^8 M_\odot$, which are too massive for seeding stellar originated black hole progenitors as the haloes are formed. We shall leave these topics for further study.

ACKNOWLEDGEMENTS

The resimulations used in this work and the MassiveBlack simulation were run on the Cray XT5 supercomputer Kraken at the National Institute for Computational Sciences. We acknowledge support from Moore foundation which enabled us to perform the data analysis at the McWilliams Center of Cosmology at Carnegie

Mellon University. This research has been funded by the National Science Foundation (NSF) PetaApps programme, OCI-0749212 and by NSF AST-1009781. The visualizations were produced using GAEPSI (Feng et al. 2011).

REFERENCES

- Abazajian K. N. et al., 2009, *ApJS*, 182, 543
 Abel T., Bryan G. L., Norman M. L., 2000, *ApJ*, 540, 39
 Agertz O. et al., 2007, *MNRAS*, 380, 963
 Alvarez M. A., Wise J. H., Abel T., 2009, *ApJ*, 701, L133
 Anglés-Alcázar D., Davé R., Özel F., Oppenheimer B. D., 2014, *ApJ*, 782, 84
 Begelman M. C., Volonteri M., Rees M. J., 2006, *MNRAS*, 370, 289
 Bellovary J., Volonteri M., Governato F., Shen S., Quinn T., Wadsley J., 2011, *ApJ*, 742, 13
 Bellovary J., Brooks A., Volonteri M., Governato F., Quinn T., Wadsley J., 2013, *ApJ*, 779, 136
 Bonoli S., Marulli F., Springel V., White S. D. M., Branchini E., Moscardini L., 2009, *MNRAS*, 396, 423
 Booth C. M., Schaye J., 2009, *MNRAS*, 398, 53
 Booth C. M., Schaye J., 2010, *MNRAS*, 405, L1
 Booth C. M., Schaye J., 2013, *Sci. Rep.*, 1738, doi:10.1038/srep01738
 Bournaud F., Dekel A., Teyssier R., Cacciato M., Daddi E., Juneau S., Shankar F., 2011, *ApJ*, 741, L33
 Bromm V., Coppi P. S., Larson R. B., 1999, *ApJ*, 527, L5
 Cattaneo A., Teyssier R., 2007, *MNRAS*, 376, 1547
 Choi J.-H., Shlosman I., Begelman M. C., 2013, *ApJ*, 774, 149
 Ciotti L., Ostriker J. P., 2007, *ApJ*, 665, 1038
 Costa T., Sijacki D., Trenti M., Haehnelt M., 2014, *MNRAS*, 439, 2146
 Davis M., Efstathiou G., Frenk C. S., White S. D. M., 1985, *ApJ*, 292, 371
 Debuhr J., Quataert E., Ma C.-P., 2011, *MNRAS*, 412, 1341
 Dehnen W., Aly H., 2012, *MNRAS*, 425, 1068
 Dekel A. et al., 2009, *Nature*, 457, 451
 Di Matteo T., Springel V., Hernquist L., 2005, *Nature*, 433, 604
 Di Matteo T., Colberg J., Springel V., Hernquist L., Sijacki D., 2008, *ApJ*, 676, 33
 Di Matteo T., Khandai N., DeGraf C., Feng Y., Croft R. A. C., Lopez J., Springel V., 2012, *ApJ*, 745, L29
 Dubois Y., Devriendt J., Slyz A., Teyssier R., 2012, *MNRAS*, 420, 2662
 Dubois Y., Pichon C., Devriendt J., Silk J., Haehnelt M., Kimm T., Slyz A., 2013, *MNRAS*, 428, 2885
 Fan X. et al., 2001, *AJ*, 122, 2833
 Fan X. et al., 2003, *AJ*, 125, 1649
 Fan X. et al., 2004, *AJ*, 128, 515
 Fan X. et al., 2006, *AJ*, 131, 1203
 Fanidakis N., Macciò A. V., Baugh C. M., Lacey C. G., Frenk C. S., 2013, *MNRAS*, 436, 315
 Feng Y. et al., 2011, *ApJS*, 197, 18
 Gao L., White S. D. M., Jenkins A., Frenk C. S., Springel V., 2005, *MNRAS*, 363, 379
 Gaspari M., Melioli C., Brighenti F., D’Ercole A., 2011, *MNRAS*, 411, 349
 Gingold R. A., Monaghan J. J., 1977, *MNRAS*, 181, 375
 Hayes J. C., Norman M. L., Fiedler R. A., Bordner J. O., Li P. S., Clark S. E., ud-Doula A., Mac Low M.-M., 2006, *ApJS*, 165, 188
 Hobbs A., Power C., Nayakshin S., King A. R., 2012, *MNRAS*, 421, 3443
 Hopkins P. F., 2013, *MNRAS*, 428, 2840
 Hopkins P. F., Quataert E., 2010, *MNRAS*, 407, 1529
 Husband K., Bremer M. N., Stanway E. R., Davies L. J. M., Lehnert M. D., Douglas L. S., 2013, *MNRAS*, 432, 2869
 Jeon M., Pawlik A. H., Greif T. H., Glover S. C. O., Bromm V., Milosavljević M., Klessen R. S., 2012, *ApJ*, 754, 34
 Jiang L. et al., 2009, *AJ*, 138, 305
 Johansson P. H., Naab T., Burkert A., 2008, *Astron. Nachr.*, 329, 956
 Khandai N., Feng Y., DeGraf C., Di Matteo T., Croft R. A. C., 2012, *MNRAS*, 423, 2397
 Kim S. et al., 2009, *ApJ*, 695, 809

- Koushiappas S. M., Bullock J. S., Dekel A., 2004, *MNRAS*, 354, 292
- Latif M. A., Schleicher D. R. G., Schmidt W., Niemeyer J., 2013, *MNRAS*, 433, 1607
- Li Y. et al., 2007, *ApJ*, 665, 187
- Lodato G., Natarajan P., 2006, *MNRAS*, 371, 1813
- Lucy L. B., 1977, *AJ*, 82, 1013
- McCarthy I. G., Schaye J., Bower R. G., Ponman T. J., Booth C. M., Dalla Vecchia C., Springel V., 2011, *MNRAS*, 412, 1965
- Mayer L., Kazantzidis S., Escala A., Callegari S., 2010, *Nature*, 466, 1082
- Milosavljević M., Couch S. M., Bromm V., 2009, *ApJ*, 696, L146
- Monaghan J. J., 2000, *J. Comput. Phys.*, 159, 290
- Morganson E. et al., 2012, *AJ*, 143, 142
- Morris J. P., 1996, *Publ. Astron. Soc. Aust.*, 13, 97
- Mortlock D. J. et al., 2011, *Nature*, 474, 616
- Nakamura F., Umemura M., 2001, *ApJ*, 548, 19
- Novak G. S., Ostriker J. P., Ciotti L., 2012, *MNRAS*, 427, 2734
- Park K., Ricotti M., 2011, *ApJ*, 739, 2
- Park K., Ricotti M., 2012, *ApJ*, 747, 9
- Pelupessy F. I., Di Matteo T., Ciardi B., 2007, *ApJ*, 665, 107
- Price D. J., 2008, *J. Comput. Phys.*, 227, 10040
- Price D. J., 2012, *J. Comput. Phys.*, 231, 759
- Priddey R. S., Ivison R. J., Isaak K. G., 2008, *MNRAS*, 383, 289
- Read J. I., Hayfield T., Agertz O., 2010, *MNRAS*, 405, 1513
- Romano-Diaz E., Shlosman I., Trenti M., Hoffman Y., 2011, *ApJ*, 736, 66
- Schaye J., Dalla Vecchia C., 2008, *MNRAS*, 383, 1210
- Schuessler I., Schmitt D., 1981, *A&A*, 97, 373
- Sijacki D., Springel V., Haehnelt M. G., 2009, *MNRAS*, 400, 100
- Springel V., 2005, *MNRAS*, 364, 1105
- Springel V., Hernquist L., 2002, *MNRAS*, 333, 649
- Springel V., Hernquist L., 2003, *MNRAS*, 339, 289
- Springel V., Di Matteo T., Hernquist L., 2005, *MNRAS*, 361, 776
- Tanaka T., Haiman Z., 2009, *ApJ*, 696, 1798
- Tanaka T. L., Li M., Haiman Z., 2013, *MNRAS*, 435, 3559
- Volonteri M., Rees M. J., 2005, *ApJ*, 633, 624
- Wadsley J. W., Veeravalli G., Couchman H. M. P., 2008, *MNRAS*, 387, 427
- Willott C. J., Omont A., Bergeron J., 2013, *ApJ*, 770, 13
- Wurster J., Thacker R. J., 2013, *MNRAS*, 431, 2513
- Yoshida N., Sokasian A., Hernquist L., Springel V., 2003, *ApJ*, 598, 73

This paper has been typeset from a \LaTeX file prepared by the author.